



**HAL**  
open science

# A creep model with different properties under tension and compression - Applications to refractory materials

Lucas Teixeira, Jean Gillibert, Thomas Sayet, Eric Blond

## ► To cite this version:

Lucas Teixeira, Jean Gillibert, Thomas Sayet, Eric Blond. A creep model with different properties under tension and compression - Applications to refractory materials. *International Journal of Mechanical Sciences*, 2021, 212, 10.1016/j.ijmecsci.2021.106810 . hal-03351489

**HAL Id: hal-03351489**

**<https://hal.science/hal-03351489v1>**

Submitted on 16 Oct 2023

**HAL** is a multi-disciplinary open access archive for the deposit and dissemination of scientific research documents, whether they are published or not. The documents may come from teaching and research institutions in France or abroad, or from public or private research centers.

L'archive ouverte pluridisciplinaire **HAL**, est destinée au dépôt et à la diffusion de documents scientifiques de niveau recherche, publiés ou non, émanant des établissements d'enseignement et de recherche français ou étrangers, des laboratoires publics ou privés.



Distributed under a Creative Commons Attribution - NonCommercial 4.0 International License

## A Creep Model with Different Properties Under Tension and Compression – Applications to Refractory Materials

Lucas Teixeira, Jean Gillibert, Thomas Sayet, Eric Blond

*Univ. Orléans, Univ. Tours, INSA-CVL, LaMé  
8 Rue Léonard de Vinci, 45072, Orléans, France*

---

### Abstract

Refractories are materials designed to work at high temperatures, and are applied in steel making, cement making, aerospace engineering, and other fields where a combination of chemical and mechanical stability is paramount. Due to such high temperature applications, creep strains play an important role in the mechanical performance of refractories, that often present an asymmetric behavior, i.e., different creep strain rates under tension and compression. The aim of this work is to propose an asymmetric creep model that can be used to simulate the time-dependent non-linear primary and secondary creep behavior of refractories at high temperature. The proposed model uses a split of the stress tensor into positive and negative parts and further calculation of the contribution of each stress sign to the overall strain rate using a weighted average over the equivalent stresses. An experimental procedure is proposed in order to identify the tensile and compressive parameters of an alumina-spinel refractory used in steel ladle linings, using a Brazilian test and a subset-based Digital Image Correlation (DIC) technique, for a temperature of 1300 °C.

*Keywords:* Asymmetric Creep, Refractories, Finite Elements, Modeling

---

## 1 List of Symbols

$\underline{\underline{\sigma}}$	Second rank stress tensor
$\sigma_{eq}$	Von Mises equivalent stress
$\sigma_x$	Stress in direction $x$
$\sigma_y$	Stress in direction $y$
$f_y$	Yield stress
$\underline{\underline{s}}$	Second rank deviatoric stress tensor
$\sigma_t$	Tensile strength
$\sigma_c$	Compression strength
$\varepsilon_x$	Total strain in direction $x$
$\varepsilon_y$	Total strain in direction $y$
$p$	Equiv. creep (viscoplastic) strain
$\underline{\underline{\dot{\varepsilon}}}^{cr}$	Second rank creep (viscoplastic) strain rate tensor
$E$	Young's modulus
$\nu$	Poisson's ratio
$A, n, m$	Temperature dependent creep parameters
$w$	Weights
$e$	Sample's thickness
$\phi_s$	Sample's diameter
$\phi_j$	Jaws' diameter
$\underline{\underline{I}}$	Identity matrix
$Tr()$	Trace
$\langle \rangle$	Macauly brackets
$x^\pm$	Positive and negative parts of variable $x$
$F$	Force
$t$	Time

### 3 1. Introduction

4 Refractories are materials designed to work at highly aggressive environ-  
5 ments, and need to resist to thermo-mechanical stresses and strains, corrosion  
6 and erosion at temperatures that can reach over 2000 °C (Banerjee, 2004). In  
7 the production of steel, cement, glass, copper, between other materials processed  
8 at high temperatures, the goal of refractory linings is to protect the vessels used  
9 in the production process, normally made of steel, from overheating and conse-  
10 quent mechanical failure, as well as to control the heat losses from the process  
11 (Schacht, 2004).

12 The transformation of raw materials into finished steel products involve high  
13 temperature processes, and different vessels lined with refractories are used to  
14 contain the molten metals, such as blast furnaces, basic oxygen furnaces (BOFs),  
15 electric arc furnaces (EAFs), ladles and tundishes. Among those vessels, the  
16 steel ladle has a considerable importance, since it is used in the secondary met-  
17 allurgy, where a considerable amount of time and financial resources have al-  
18 ready been previously employed on the production process, and is responsible  
19 for a non-negligible consumption of refractories (Dutta & Chokshi, 2020). The  
20 integrity of the ladle is of central importance to the safety of the production  
21 site, since it transits between other equipments and workers, carrying molten  
22 steel, and a failure can lead to serious consequences.

23 Figure 1a shows a cutaway view of a steel ladle, and Figure 1b shows a  
24 schematic representation of the top view of one ring of a ladle lining. The choice  
25 of the refractories to be applied in each layer of the lining greatly influences the  
26 temperature distribution in the ladle, therefore playing also a crucial role on  
27 its thermo-mechanical behavior (Volkova & Janke, 2005) and on the energy  
28 consumption.

29 An important phenomena to be considered in the design of the steel ladle is  
30 the creep and stress relaxation of the refractory lining. The absence of a non-  
31 linear viscoplastic behavior can lead to stress values that can't be supported by  
32 the vessel, causing a mechanical failure. Nevertheless, if the material presents

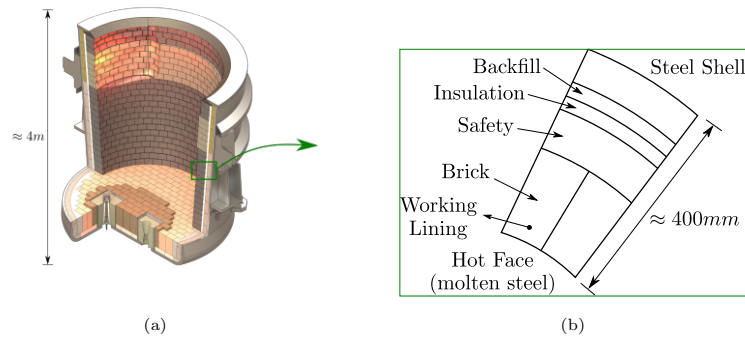


Figure 1: Example of a steel ladle. (a) Cutaway view showing the refractory linings. (b) Schematic representation of a line ring, top view.

33 excessive creep, it will have a considerable reduction on its size caused by the  
 34 compression stresses at the hot face. During the cooling of the ladle, joints  
 35 may open, making the lining loose and allowing for steel infiltration in posterior  
 36 production cycles. Therefore, the design of the refractory lining and of the steel  
 37 shell can benefit from a numerical model that can predict more accurately the  
 38 stress and strain variations over time, and the effect of thermal cycles can be  
 39 taken into account to maximize the vessel's life.

40 Due to the complexity of their mechanical behavior, the modeling and sim-  
 41 ulation of refractory materials has often been restricted to the application of  
 42 simple constitutive models, in some cases even neglecting the well known non-  
 43 linearity of the material (Jin et al., 2011). In other cases, creep models have  
 44 been applied to simulate the thermo-mechanics of refractories, but considering a  
 45 symmetric behavior and using the compressive mechanical properties (Jin et al.,  
 46 2020). There were also attempts to use a Drucker-Prager-based creep model to  
 47 simulate the effect of the material's asymmetry of RH-degassers lining behavior,  
 48 but the authors concluded that this model might not be ideal and that more  
 49 complex representation of the actual behavior should probably be used (Jin et  
 50 al., 2015).

51 In this work, an asymmetric creep model is proposed, which is able to repre-

52 sent the different behavior that refractory materials present under tension and  
53 compression. The main goal is to obtain a relatively simple constitutive model,  
54 that can have the material parameters identified using the least possible num-  
55 ber of mechanical tests, due to the need to characterize the material at several  
56 temperatures, which requires a high time and energy consumption. With the  
57 proposed model, the lifetime of refractory materials can be predicted more ac-  
58 curately than the using current engineering practice (linear elastic or symmetric  
59 creep models), since it accounts for the significant increase in the creep strain  
60 rate when tensile loads are present in the lining. Similarly, the model allows  
61 for a better comparison between the performance of products with different  
62 shapes and compositions, reducing field trials and improving the availability of  
63 the equipments.

64 Section 2 provides a description of the current creep models available in the  
65 literature, explaining what are the missing features when the simulation of re-  
66 fractory materials need to be done. Section 3 describes the proposed model,  
67 and comments on possible numerical difficulties that can arise when implement-  
68 ing it, as well as numerical strategies that can be used to mitigate them. Sec-  
69 tion 4 presents numerical simulations used to theoretically validate the proposed  
70 model. Section 5 describes the high temperature experimental procedure used  
71 to characterize the material, with a detailed explanation of the reason why the  
72 Brazilian test method was used. Finally, Section 6 presents the identification of  
73 the material parameters of an alumina-spinel brick used in steel ladles.

## 74 **2. Symmetric and asymmetric creep models**

75 The creep behavior of ceramic materials can be split in three stages. The  
76 first stage, called primary creep, presents a time-dependent strain rate which  
77 decreases with time. In the secondary creep stage, the strain rate is considered to  
78 be constant, and an approximate equilibrium between hardening and softening  
79 processes can be assumed (Naumenko & Altenbach, 2007). Finally, in the third  
80 creep stage, the strain rate increases with time until the failure of the material

81 (Jin et al., 2014).

### 82 2.1. Symmetric creep models

83 One of the most traditional creep models available in the literature is based  
84 on the one-dimension Norton-Bailey’s law, known on its multi-dimensional ver-  
85 sion as Odqvist’s law (Lemaître & Chaboche, 1990), which relates the creep  
86 strain rate  $\underline{\underline{\dot{\epsilon}}}^{cr}$  to the stresses using the following equation:

$$\underline{\underline{\dot{\epsilon}}}^{cr} = \frac{3}{2} \underline{\underline{s}} A \sigma_{eq}^{n-1} p^m \quad (1)$$

87 where  $\underline{\underline{s}}$  is the deviatoric component of the stress tensor,  $\sigma_{eq}$  is the von Mises  
88 equivalent stress,  $p$  is the equivalent viscoplastic strain (sometimes refered to as  
89 equivalent creep strain) and  $A$ ,  $n$ , and  $m$  are temperature dependent material  
90 parameters. For the case of secondary creep,  $m = 0$ . The Norton-Bailey’s  
91 law have been extensively used to characterize refractory materials, due to its  
92 simplicity and good fitness to experimental results (Jin et al., 2014; Samadi  
93 et al., 2020; Schachner et al., 2019; Sidi Mammam et al., 2016; Teixeira et al.,  
94 2020).

95 If an elastic region needs to be considered in the model, a simple modification  
96 in Equation 1 can be done to take it into consideration (Lemaître & Chaboche,  
97 1990):

$$\underline{\underline{\dot{\epsilon}}}^{cr} = \frac{3}{2} \frac{\underline{\underline{s}}}{\sigma_{eq}} A \langle \sigma_{eq} - f_y \rangle^n p^m \quad (2)$$

98 where  $f_y$  is the yield stress and  $\langle \ \rangle$  are the Macaulay brackets.

99 It should be noted that different uniaxial laws other than Norton-Bailey’s law  
100 can be applied to relate the stresses to the creep strains (Lemaître & Chaboche,  
101 1990). The choice of which law should be used depends on how accurately it  
102 fits the mechanical tests.

### 103 2.2. Asymmetric creep models

104 As can be noticed in Equations 1 and 2, the Norton-Bailey creep model  
105 is not able to represent materials with different behaviors under tension and

106 compression (asymmetric creep).

107 The asymmetry in the material's response was approached by Altenbach  
108 (2001) using a creep strain rate formulation that depends on three linear inde-  
109 pendent invariants of the stress tensor. Alternatively, Mahnken (2003) proposed  
110 an asymmetric creep model that uses a scalar variable expressed in terms of the  
111 ratio of the second and third invariants of the deviatoric stress tensor, called  
112 stress mode angle in the octahedral plane in the deviatoric stress space.

113 Although these models are mathematically consistent and were successfully  
114 applied, they present the inconvenient to require a considerable number of ex-  
115 periments to determine the creep parameters, since tension and compression  
116 behaviors are not decoupled. For the case of refractories, that need to be char-  
117 acterized at several temperatures, this represents a limitation.

118 More recently, Samadi et al. (2021) coupled the asymmetric primary creep  
119 behavior of refractories with a damage model. In this model, the equation for  
120 the creep strain rate is selected according to the sign of the principal stresses,  
121 without any particular weighting strategy, and the equations are solved using  
122 an explicit integration scheme.

123 To account for the asymmetric creep of refractories, Blond et al. (2005)  
124 extended the Norton-Bailey's model, using a split of the principal stress vec-  
125 tors into a positive and a negative parts, to propose a secondary creep model,  
126 resulting in:

$$\underline{\underline{\sigma}} = \langle \underline{\underline{\sigma}} \rangle - \langle -\underline{\underline{\sigma}} \rangle \quad (3)$$

127 This split results in the definition of the model in terms of independent ten-  
128 sion and compression parameters. In this sense, the two parts of the deviatoric  
129 stress tensor are given by:

$$\underline{\underline{s}}^{\pm} = \langle \pm \underline{\underline{\sigma}} \rangle - \frac{1}{3} Tr(\langle \pm \underline{\underline{\sigma}} \rangle) \underline{\underline{I}} \quad (4)$$

130 where the indexes  $\pm$  indicate the positive and negative parts of the variables,



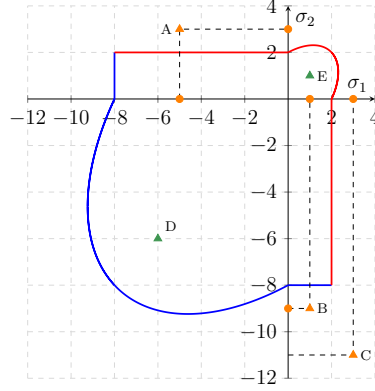


Figure 2: Yield surface of Blond's model.

131 respectively. The equivalent von Mises stresses are, then:

$$\sigma_{eq}^{\pm} = \sqrt{\frac{3}{2} \underline{\underline{s}}^{\pm} : \underline{\underline{s}}^{\pm}} \quad (5)$$

132 resulting in a viscoplastic strain rate of the form:

$$\underline{\underline{\dot{\epsilon}}}_{cr} = \frac{3}{2} \frac{\underline{\underline{s}}^+}{\sigma_{eq}} A^+ \langle \sigma_{eq}^+ - f_y^+ \rangle^{n^+} - \frac{3}{2} \frac{\underline{\underline{s}}^-}{\sigma_{eq}} A^- \langle \sigma_{eq}^- - f_y^- \rangle^{n^-} \quad (6)$$

133 where  $A^{\pm}$  and  $n^{\pm}$  are material's constants in tension (+) and compression (-).

134 Figure 2 shows a representation of Blond's model in the 2D principal stresses  
 135 domain. In this example, the tensile yield stress is  $f_y^+ = 2$  MPa and the com-  
 136 pressive yield stress is  $f_y^- = -8$  MPa. In the figure, the stress states  $D$  and  
 137  $E$  marked as green triangles are inside the elastic region, therefore no creep is  
 138 observed.

139 Point  $A$  shows a stress state in the second quadrant, with a compressive  
 140 component in direction 1 and a tensile component in direction 2. Therefore, the  
 141 stress split described by Equation 3 results in other two stress states, shown as  
 142 circular markers. As can be seen, the point  $(-5, 0)$  is in the elastic region, so no  
 143 creep is expected for the compressive component. On the other hand, the point  
 144  $(0, 3)$  lays outside the elastic region, so the first term of the right hand side of

145 Equation 6 is activated, and creep in tension is observed.

146 Point B corresponds to the opposite situation, i.e., creep is activated in  
147 compression but not in tension. The stress state represented by Point C results  
148 in creep in both tension and compression.

149 From Figure 2, it is also evident that Blond's yield surface presents singular-  
150 ities at the points where it crosses axis 1 and 2, as well as in the corners present  
151 in the second and fourth quadrants. When the structure being modeled has  
152 stress states close to these singularities, difficulty in the convergence may arise.  
153 Nevertheless, this should not be a problem if the yield stress is equal to zero,  
154 i.e., the material starts to creep as soon as a load of any magnitude is imposed,  
155 which is often the case for refractories (Jin et al., 2014).

156 One of the main advantages of this model is that the material's parameters  
157 for tensile and compression creep are completely independent, therefore they can  
158 be identified separately. This gives flexibility to fit the creep flow calculations  
159 to a large range of strain rates observed in experiments.

160 Nevertheless, the validity of the stress split hypothesis needs to be verified,  
161 and this model presents the characteristic of making a sum between two terms  
162 (positive and negative strain rates) that depend on the equivalent stress. The  
163 consequence of this fact is that, if this model is used with identical properties  
164 in tension and in compression, the resulting viscoplastic strain rate is not the  
165 same as the one obtained with a symmetric model. Although this is not nec-  
166 essarily a limitation, in some cases it can be desirable to have a model that is  
167 an interpolation of the tension and the compression material behaviors, without  
168 this intrinsic orthotropy.

169 As remarked by Esposito and Bonora (2011), in many applications the pri-  
170 mary creep of materials can't be neglected, since a considerable part of the al-  
171 lowable design strain occurs in this stage. This is the case of the alumina-spinel  
172 material studied in this work, as it is evident by the creep curves previously  
173 published by Samadi et al. (2020) and Teixeira et al. (2020).

174 **3. Proposition of an asymmetric creep model considering primary**  
 175 **and secondary creep stages**

176 *3.1. Model description*

177 In this work, to represent the primary and secondary creep behaviors of  
 178 refractory materials, Equation 1 was adapted following the same principle of  
 179 the split of the stress tensor in a positive and a negative part, as used by Blond  
 180 et al. (2005).

181 The proposed model also differentiates from Blond's model in the way to  
 182 consider the different contributions of the compression and tensile characteristics  
 183 of the material. After the decomposition of the stress tensor, the deviatoric and  
 184 equivalent stresses are calculated for each part (positive and negative) using  
 185 Equations 4 and 5, respectively, such as in the model proposed by Blond et al.  
 186 (2005).

187 Nevertheless, instead of using  $\underline{s}^\pm$  and  $\sigma_{eq}^\pm$  to directly calculate the positive  
 188 and negative viscoplastic strain rates (Equation 6), these values are used to  
 189 calculate relative weights that each part of the stress tensor have on the total  
 190 equivalent stress, using the relation:

$$w^\pm = \frac{\sigma_{eq}^\pm}{\sigma_{eq}} \quad (7)$$

191 Each portion of the viscoplastic strain rate is calculated as a function of  
 192 the total deviatoric and equivalent stresses (using the full stress tensor, before  
 193 the decomposition into positive and negative parts) and the respective material  
 194 properties:

$$\underline{\dot{\epsilon}}^{cr\pm} = f(\underline{s}, \sigma_{eq}, A^\pm, n^\pm, m^\pm) \quad (8)$$

Later, each part of the viscoplastic strain rate is weighted by the values cal-  
 culated using Equation 7. Therefore, the viscoplastic strain rate of the proposed  
 asymmetric creep model is given by:

$$\underline{\dot{\epsilon}}^{cr} = w^+ \cdot \frac{3}{2} \frac{\underline{s}}{\sigma_{eq}} A^+ \langle \sigma_{eq} - f_y^+ \rangle^{n^+} p^{m^+} - w^- \cdot \frac{3}{2} \frac{\underline{s}}{\sigma_{eq}} A^- \langle \sigma_{eq} - f_y^- \rangle^{n^-} p^{m^-} \quad (9)$$

195 This model is also similar to the one developed by Mahnken (2003), in the  
 196 sense that it proposes a weighted calculation of the creep strain rate. Never-  
 197 theless, the model proposed here can be considered to be more straightforward,  
 198 and it also requires less parameters to characterize the creep behavior of a given  
 199 material, which is an important advantage. This model was implemented in an  
 200 Abaqus UMAT subroutine, and examples of calculations are shown in the next  
 201 sections. The integration algorithm according to Benallal et al. (1988) was used  
 202 in this subroutine.

203 It should be noted that, when the material presents primary creep under  
 204 compression and secondary creep under tension, such as in the case of the  
 205 alumina-spinel brick,  $m^- = 0$  in Equation 9. To summarize, Figure 3 presents  
 206 flow charts corresponding to the algorithm proposed by Blond et al. (2005) (full  
 207 lines) and the algorithm proposed in this work (dashed lines).

### 208 3.2. Numerical difficulties associated with primary creep

209 At the beginning of a structural simulation, when the load was not yet  
 210 applied, the strain in the simulated body is assumed to be zero, unless otherwise  
 211 stated. In this situation, it is reasonable to assume that the equivalent creep  
 212 strain is  $p = 0$ . Examining Equation 9 and taking into account that the variable  
 213  $m$  can only take negative values, it is easy to deduce that:

$$\lim_{p \rightarrow 0} \underline{\underline{\dot{\epsilon}^{cr}}} = 0 \quad (10)$$

214 Therefore, the equivalent viscoplastic strain can't be defined as zero at time  
 215  $t = 0$ , since this would result in the absence of creep strain in the subsequent  
 216 time step, independently of the applied load.

217 The first solution to this problem is to define a low non-zero initial value  
 218 for  $p$ . Nevertheless, it is not always clear which value should be used, since the  
 219 convergence of the simulation is highly dependent on it. For example, consider a  
 220 case where only compression creep is applied and  $f_y = 0$ . Equation 9 becomes:

$$\underline{\underline{\dot{\epsilon}^{cr}}} = \frac{3}{2} s A^- \sigma_{eq}^{(n^- - 1)} p^{m^-} \quad (11)$$

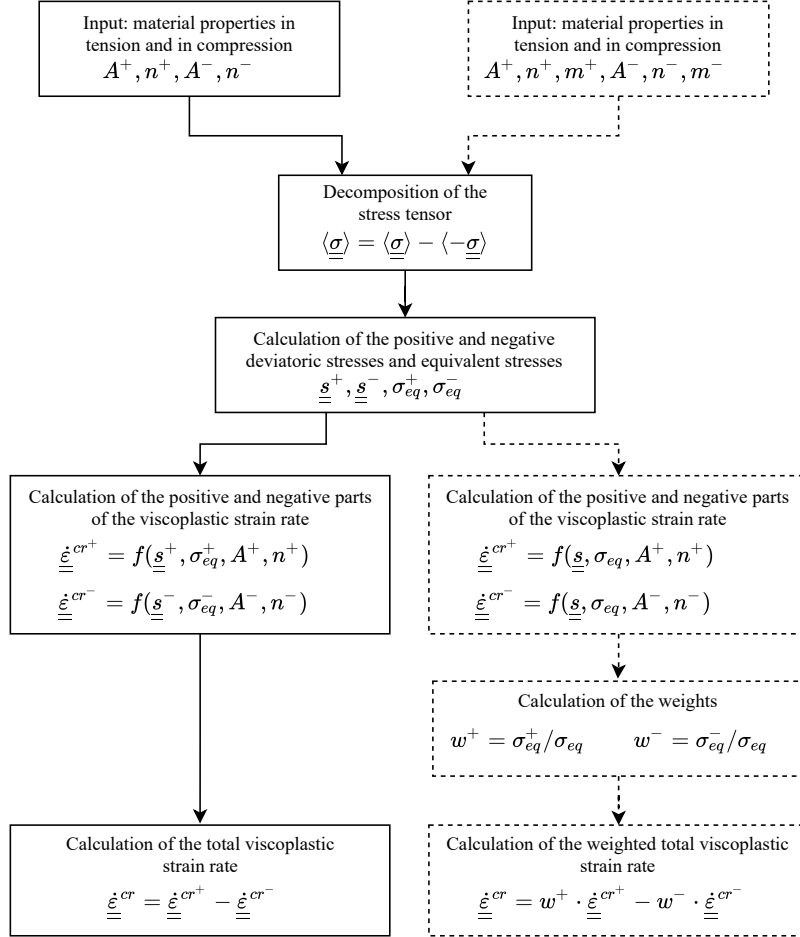


Figure 3: Asymmetric creep model algorithms. Blond et al. (2005) (full lines) and the proposition of this work(dashed lines)

221 Supposing  $\underline{s}$  and  $\sigma_{eq}$  to have an order of magnitude of 10,  $A \approx 1 \times 10^{-10}$ ,  
 222  $m \approx -2$ ,  $n \approx 2$  and an initial approximation of  $p = 1 \times 10^{-15}$ , the resulting creep  
 223 strain rate would be  $\underline{\dot{\epsilon}}^{cr} \approx 1 \times 10^{22}$ . A high value of initial creep strain rate is

224 expected from primary creep, but at this rate of strain, the integration algorithm  
225 would have to use an extremely low [time step value](#) in order to converge, [which](#)  
226 is not practical.

227 It can be concluded that [an initial equivalent viscoplastic strain value](#) should  
228 be used so that it is small enough to do not decrease the accuracy of the solution  
229 and large enough to allow the convergence in a reasonable time frame. This value  
230 depends on the material properties, the applied loads, the boundary conditions  
231 and on the time stepping used during the solution, and can be considerably  
232 difficult to estimate.

233 To improve the convergence of the model, the following actions can be taken:

- 234 1. Given the material properties and boundary conditions of the problem, an  
235 initial value for the equivalent creep strain  $p_{t=0}$  needs to be determined.  
236 The convergence of the initial steps of the model is tested, using a small  
237 time increment. If necessary,  $p_{t=0}$  should be increased.
- 238 2. The time step increment should be small during the first seconds of load-  
239 ing, since the primary creep curve can be steep at the beginning. It can  
240 be interesting to brake the initial steps into smaller ones, to allow a finer  
241 control of the time increment.
- 242 3. Even when the initial moments of primary creep are past, the maximum  
243 increment of time should be limited to reasonable values, since the auto-  
244 matic time stepping control present in some FEA software can attempt  
245 to increase it beyond the convergence limit of the integration algorithm.  
246 Even if the software is able to converge, it can take many iterations to  
247 finish a step, leading to slower computations.

248 Even if those measures are taken, the simulation can still diverge due to  
249 a rapid change in the creep strain rate, specially for the case where tensile  
250 loads are meaningful. To limit this problem, in the UMAT subroutine used to  
251 implement the creep models developed in this work, [a variable was implemented](#)  
252 [to control](#) the convergence of the integration algorithm. If the algorithm does  
253 not converge, the subroutine automatically returns to the previous converged

254 iteration, and tries a time step that is half the previous attempt. This action is  
 255 only effective if the convergence problem is related to the integration algorithm  
 256 of the constitutive equations, not to the global Newton-Raphson integration  
 257 scheme.

#### 258 4. Numerical simulations using the proposed asymmetric creep model

259 To evaluate the capabilities of the proposed asymmetric model, a set of  
 260 numerical simulations is presented, in increasing order of complexity. The goal  
 261 of these simulations is to verify if the model presents the expected behavior when  
 262 subjected to complex load cases. The material parameters used to perform these  
 263 tests are shown in Table 1. As it will become evident in the next sections, these  
 264 material parameters are close to the one corresponding to the alumina-spinel  
 265 material. It was considered that the tensile behavior of the material could be  
 266 approximated by a secondary creep model, as discussed by Teixeira et al. (2020).

Table 1: Material parameters used in the numerical simulation tests

Parameter	Compression	Tension
$E[\text{MPa}]$	30000	30000
$\nu[-]$	0.2	0.2
$\log_{10} A[\text{MPa}^{-n} \text{s}^{-1}]$	-14.16	-5.4
$n[-]$	3.96	1.5
$m[-]$	-2.74	-

267 In the simulations, four situations regarding the type of model and the ma-  
 268 terial parameters were considered:

- 269 1. Abaqus symmetric creep model using the compression properties of the  
 270 material. This configuration is commonly seen in publications related to  
 271 the creep of refractories, as previously cited.

- 272 2. Abaqus symmetric creep model using the tension properties of the mate-  
273 rial, used as a reference to compare with the asymmetric model.
- 274 3. UMAT asymmetric creep model, but using the compression properties  
275 of the material for compression and tension, to verify if the asymmetric  
276 model specializes to a symmetric one when necessary.
- 277 4. UMAT asymmetric creep model, using the corresponding properties for  
278 tension and compression.

#### 279 *4.1. Normal loads with stress reversal in two dimensions*

280 The first model corresponds to a simple two-dimensional element (Figure 4a,  
281 where  $e$  is the thickness) subjected to a load path that varies in directions  $x$  and  
282  $y$ , according to Figure 4b. The maximum tensile stress is  $\sigma_t = 0.2$  MPa, and  
283 the minimum compression stress is  $\sigma_c = -2.0$  MPa. Figures 4c and 4d show  
284 the time periods for which the stresses are kept in the sample.

285 Although this is a simple model, it represents a situation where, during  
286 the loading cycle, there are moments where both principal stresses are positive  
287 (Point B), both are negative (Point D), and when there is a composition of  
288 positive and negative stresses at the same integration point (Points C and E).  
289 Therefore, the simulation is useful to show the difference between a symmetric  
290 and an asymmetric model, as well as the effect of the loading history. For this  
291 model, an extra curve using the tension material parameters for both tension  
292 and compression material laws is also presented.

293 Figure 5 shows the accumulated viscoplastic strains computed in each of the  
294 situation previously described. It is possible to observe that, when the same  
295 properties are used for tension and compression, the UMAT provides the same  
296 results as a symmetric model. More importantly, the asymmetric model presents  
297 an intermediate response between the tension and the compression symmetric  
298 models, as expected.

299 In Figure 5 it is clear that, until approximately 30 min, when only tension  
300 stresses are present in the element (Points A and B in Figure 4), the symmetric  
301 and asymmetric models give the same result. From that point further, when



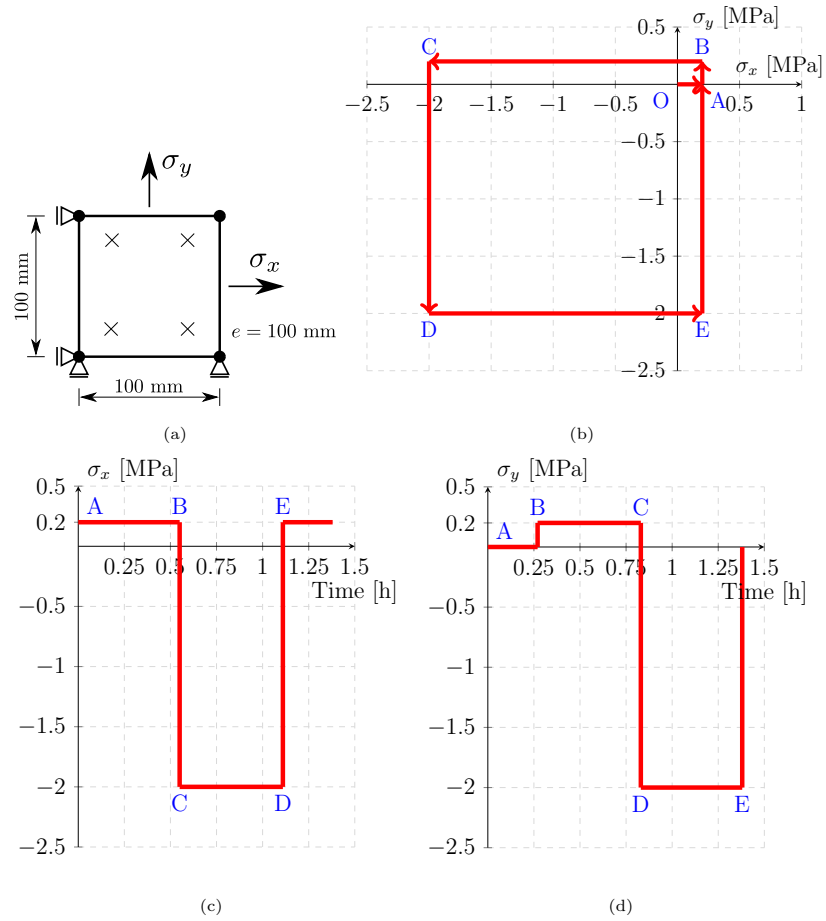


Figure 4: Stress distribution – Normal loads. (a) Simulation model. (b) Stress path. (c)  $\sigma_x$  vs Time. (d)  $\sigma_y$  vs Time.

302 an asymmetry is included in the loading (Point C in Figure 4), the model re-  
 303 sponse changes, becoming an interpolation between the tension and compression  
 304 behaviors.

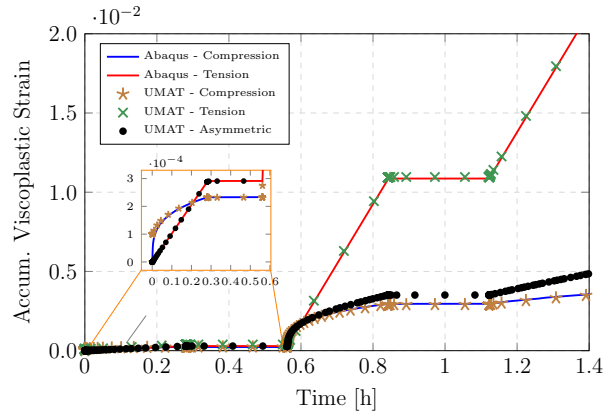


Figure 5: Accumulated viscoplastic strain – Normal loads.

305 *4.2. Brazilian test*

306 Figure 6 shows the geometry, mesh and boundary conditions used to compare  
 307 the symmetric and asymmetric models applied to a Brazilian test specimen. The  
 308 sample was discretized using linear square elements with full integration, unless  
 309 for a transition zone between the refined mesh in the contact region and the  
 310 rest of the geometry, where linear triangular elements with full integration were  
 311 used.

312 The sample was modeled with  $\phi_s = 50$  mm diameter and  $e = 40$  mm thick-  
 313 ness. Analytic rigid surfaces representing the upper and lower jaws with diam-  
 314 eters  $\phi_j = 65$  mm were used to distribute the load more evenly on the sample  
 315 and to avoid excessive stress concentrations. The same strategy was used at the  
 316 bottom part of the model to restrict the vertical displacement of the sample.  
 317 Due to the geometry and force symmetries, only half of the sample was modeled.

318 A force of  $-400$  N was applied on the model following a 30 s linear ramp,  
 319 and it was kept for two hours. This geometry and boundary conditions are the  
 320 same used for the mechanical tests at  $1300$  °C, presented in Section 5.

321 A comparison between vertical and horizontal displacements taken at the  
 322 center of the sample for the four cases is shown in Figure 7. It is possible to

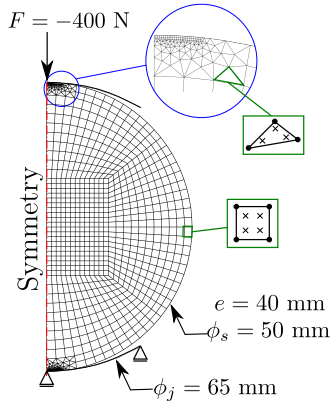


Figure 6: Brazilian test – Geometry, mesh and boundary conditions.

323 observe that, when compression curves are used in the asymmetric model, the  
 324 result is in high agreement with the symmetric model available on the software  
 325 Abaqus.

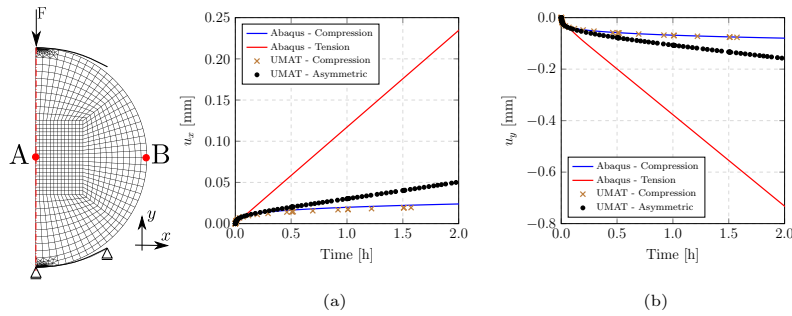


Figure 7: (a) Vertical and (b) horizontal displacements in the Brazilian test sample.

326 Figures 8 and 9 show the maximum principal stress and the minimum principal  
 327 stress on the sample, respectively, for the cases where only tension or  
 328 compression material parameters were considered (symmetric creep), and the  
 329 asymmetric case. It can be observed that the maximum tensile stress value  
 330 obtained on the sample was 0.35 MPa. Since refractory materials are less re-

331 sistant to tension, this stress limits the amount of force that can be applied  
332 before the failure of the sample. The maximum compressive stresses observed  
333 on the sample are in the range of  $-2.5$  MPa to  $-3.8$  MPa, although at the  
334 center of the sample this value does not go higher than  $-1.8$  MPa. This can be  
335 considered as a limitation of the Brazilian test when compared to uniaxial tests  
336 for the identification of material parameters, i.e., the tension and compression  
337 loads are not decoupled, therefore the material can only be safely character-  
338 ized for a smaller stress range. Nevertheless, this only represents a problem if,  
339 during operation, the actual compression stresses withstand by the material are  
340 considerably higher than the ones during the mechanical tests.

341 It should be noted that, in Figures 8 and 9, the contact zones were excluded  
342 from the results plots. This was done because, in these regions, the model can  
343 experiment stress concentrations, that makes the visualization of the plots more  
344 difficult in the other regions of the model. In a real experiment, these regions  
345 suffer from a local failure, with the crash of the grains at the contact with  
346 the jaws. This failure can normally be neglected in the experiment, but it can  
347 influence the convergence of the numerical model. For instance, the elements  
348 with higher stresses present, as a consequence, higher creep strain rate, and the  
349 model takes longer to converge due to the need of low time steps, even if the bulk  
350 part of the sample is still under low stresses. To use the proposed asymmetric  
351 model, attention should be payed to such stresses concentration areas, and they  
352 should be removed from the model, if possible.

353 When compared to a symmetric model using the compression creep prop-  
354 erties, the asymmetric model has a considerably different behavior over time  
355 regarding the strains. Figure 10 shows that, over the central line of the sam-  
356 ple, the total strain  $\varepsilon_x$ , that is mainly positive, is the same for both models at  
357 the end of loading (30 s). Nevertheless, after one hour, the strain obtained by  
358 the asymmetric model is approximately the double of the one obtained by the  
359 symmetric model, and after two hours the ratio between them is around three.  
360 The same proportional difference is observed on Figure 11 for the total strain  
361  $\varepsilon_y$ , that is compressive. This fact is due to the averaged sum of the tension

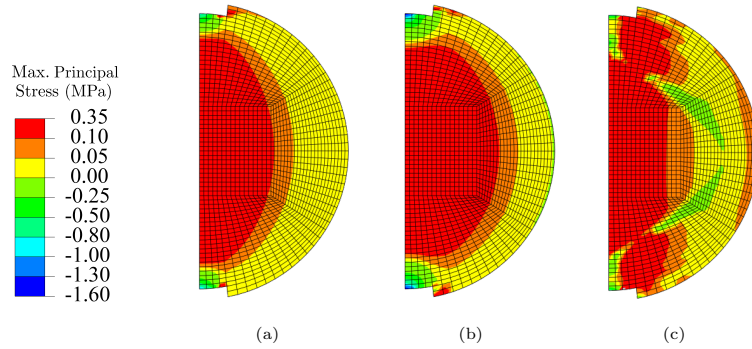


Figure 8: Maximum principal stress distribution on a Brazilian test sample. (a) compression (b) tension and (c) asymmetric material properties.

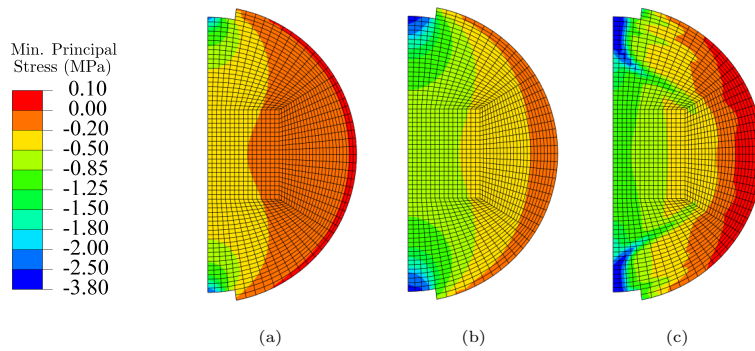


Figure 9: Minimum principal stress distribution on a Brazilian test sample. (a) compression (b) tension and (c) asymmetric material properties.

362 and compression creep strain rates applied by the asymmetric model, where the  
 363 tension part contributes to considerably increase the value of the strains.

364 Finally, Figure 12 shows the effect of the asymmetry in the accumulated vis-  
 365 coplastic strain on a Brazilian test. Once again, the proposed asymmetric model  
 366 shows an intermediary behavior between the symmetric ones, and evidences the  
 367 importance of the consideration of the different material properties in tension  
 368 and in compression.

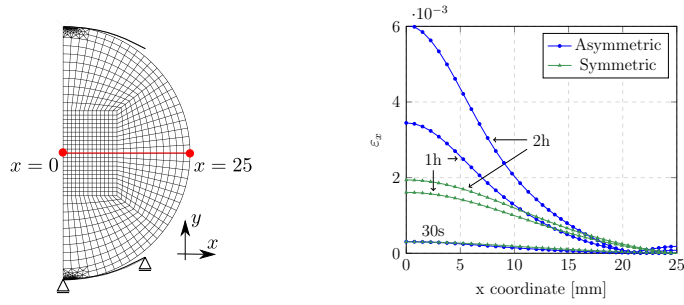


Figure 10: Variation of the total strain in direction  $x$  with time – Symmetric and asymmetric models.

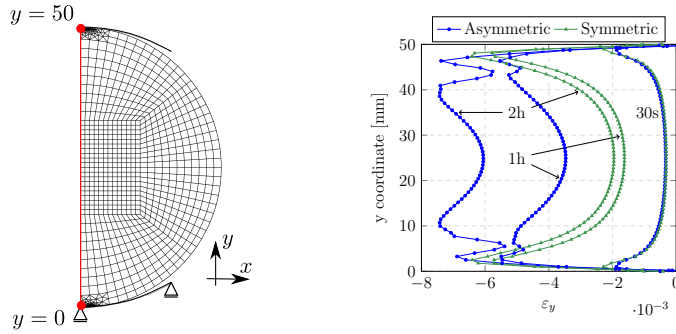


Figure 11: Variation of the total strain in direction  $y$  with time – Symmetric and asymmetric models.

369 *4.2.1. Influence of the constitutive model parameters*

370 To have a better idea on how each of the constitutive model parameters  
 371 influences the results obtained from a Brazilian test simulation, calculations  
 372 were made varying one parameter at a time around the absolute values of the  
 373 nominal properties presented on Table 1 by  $-10\%$ ,  $-20\%$ ,  $+10\%$  and  $+20\%$ .  
 374 These values are shown in Table 2. This method is not considered an accurate  
 375 sensitivity analysis, and the intention is to qualitatively understand how the  
 376 parameters influence the shape of the time-displacement curves, which is an  
 377 useful information [when an inverse identification of the parameters using real](#)

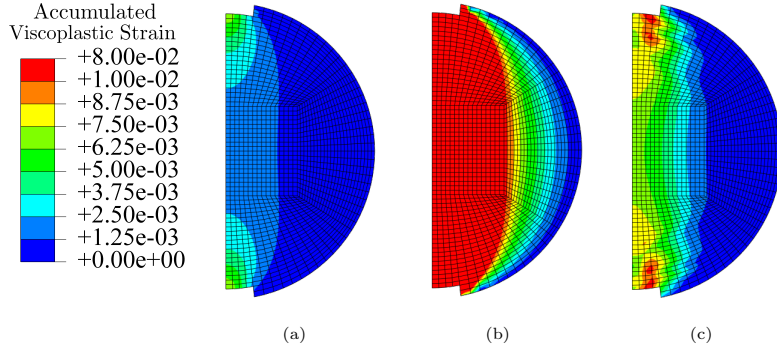


Figure 12: Accumulated viscoplastic strain distribution on a Brazilian test sample. (a) compression (b) tension and (c) asymmetric material properties.

378 experiments needs to be done. Figure 13 shows the variation of the vertical  
 379 displacement  $u_y$  of the top of the sample as a function of time, according to the  
 380 change of the parameters.

Table 2: Variation of the material parameters – Isotropic creep model

Parameter	+10%	+20%	-10%	-20%
$\log_{10} A^- [\text{MPa}^{-n} \text{s}^{-1}]$	-15.57	-16.99	-12.74	-11.32
$n^- [-]$	4.35	4.75	3.56	3.16
$m^- [-]$	-3.01	-3.28	-2.46	-2.19
$\log_{10} A^+ [\text{MPa}^{-n} \text{s}^{-1}]$	-5.94	-6.48	-4.86	-4.32
$n^+ [-]$	1.65	1.8	1.35	1.2

381 Figures 13a, 13b and 13c show the influence of the compression parameters  
 382  $A^-$ ,  $n^-$  and  $m^-$ , respectively. The curve with the variation of -20% was not  
 383 plotted, since the displacement was excessively high, due to the large influence  
 384 of this parameter in the results. It is possible to observe that parameter  $n^-$ ,  
 385 that is an exponent of the stress, has a negligible influence on the results, due to

386 the low values of stresses in this application. Parameters  $A^-$  and  $m^-$  influence  
387 mostly the beginning of the curve, changing its curvature radius, indicating that  
388 the compression stresses are predominant during the first hour, and the tensile  
389 stresses take over from this point further. This is an important conclusion, since  
390 it helps to decide in which part of the curve the identification procedure will  
391 focus, depending on the desired result.

392 Similarly,  $A^+$  has the higher influence among the tensile parameters, as can  
393 be observed in Figures 13d and 13e, although  $n^+$  starts to be influent after one  
394 hour of loading and can become more meaningful for longer periods. Contrary  
395 to the compressive parameters, the tensile parameters, specially  $A^+$ , change  
396 mainly the slope of the curve after the initial curvature has passed. Again,  
397 this remarkable separation in time between the influence of the tensile and  
398 compressive parameters facilitates the inverse identifications.

## 399 5. Experimental methodology

400 In this work, Brazilian tests were used to identify the creep parameters of  
401 an alumina-spinel material. Traditionally, Brazilian tests have been applied to  
402 study the tensile strength of concretes and geomaterials, as a replacement to  
403 direct tensile tests. As pointed by several studies, the results of a Brazilian test  
404 to calculate the tensile strength of a given material is only valid if the crack  
405 initiation is at the center of the sample, and not at the stress concentrations  
406 present at the contact points (Darvell, 1990; Fairhurst, 1964; García et al.,  
407 2017). For the applications in the current work, the position of the initiation of  
408 the crack is not important, since no fracture is expected during the test.

409 The Brazilian test was chosen for the identification of the asymmetric creep  
410 parameters due to the complexity of the stress field developed in the sample  
411 during the application of the load. As shown in Figure 14, tensile stresses  
412 are developed at the center of the sample, while compressive stresses start to  
413 increase towards its borders and shear stresses are present in the regions in  
414 contact with the upper and lower jaws. A more detailed description of the



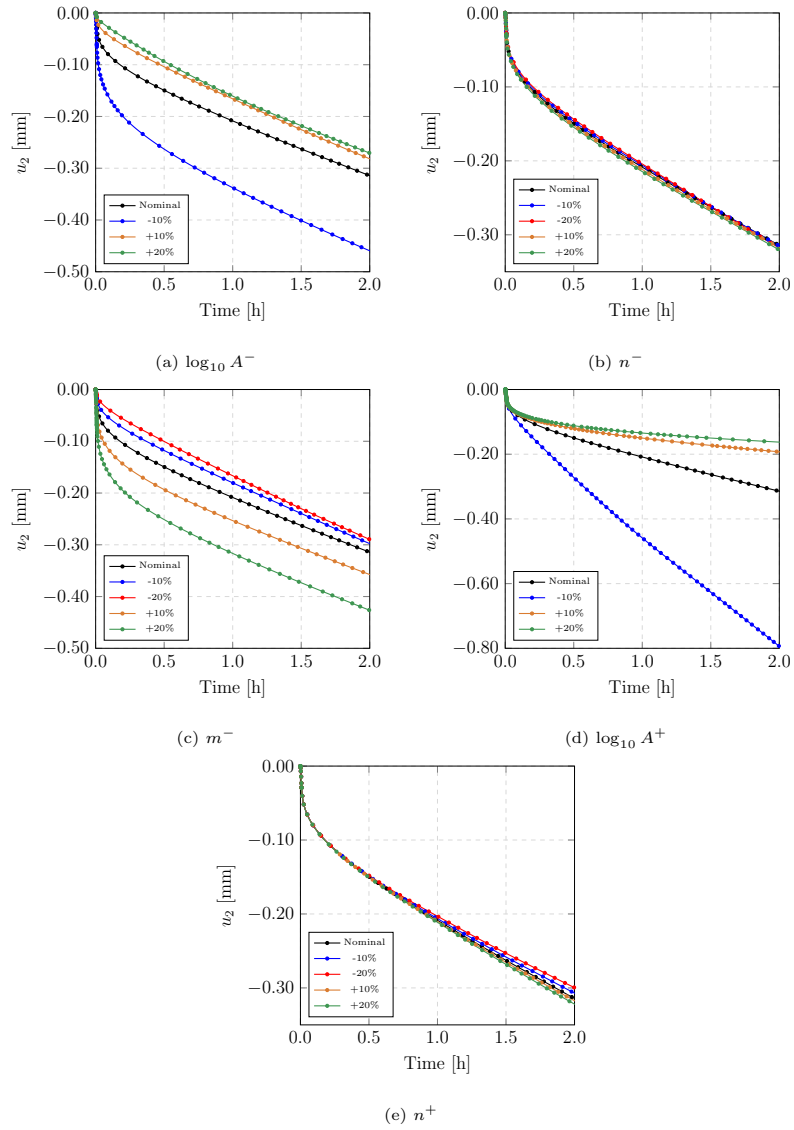


Figure 13: Change on the asymmetric creep model response due to variations of the material parameters – Brazilian test.

415 stress equations related to the Brazilian test can be found in Fahad (1996).  
416 This stress distribution is adapted to the current case, since it allows the study  
417 of the effect of the material properties under tension and compression using a  
418 single test, which considerably reduces the number of experiments that need to  
419 be performed.

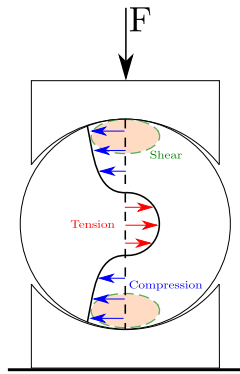


Figure 14: Stress distribution in a Brazilian test sample

420 The application of Brazilian tests to refractory materials is still limited, spe-  
421 cially regarding the characterization of creep behavior. Belrhiti et al. (2017) used  
422 this test in association to a DIC technique to characterize the mechanical be-  
423 havior of magnesia hercynite refractories used in cement rotary kilns, estimating  
424 the elastic modulus, Poisson's ratio and fracture energy at room temperature.  
425 Gazeau et al. (2015) used the Brazilian test associated with the integrated DIC  
426 technique to identify the Young's modulus and the tensile strength of plane  
427 membranes at temperatures up to 900 °C. These two applications demonstrate  
428 the potential of this method to provide various information using a single ex-  
429 perimental setup, what can result in the reduction of the required number of  
430 tests to characterize a material. This is specially important considering the cost  
431 and time demand of high temperature tests.

432 5.1. Experimental setup

433 In this work, the Brazilian test was used in association with a DIC technique.  
434 This technique is convenient for the current application, since the traditional  
435 instrumentation of testing setups at high temperatures present significant diffi-  
436 culties.

437 Previous works have given detailed information about DIC applications at  
438 high temperatures (Leplay et al., 2015; Leplay et al., 2010, 2012; Novak & Zok,  
439 2011). When pictures at high temperatures need to be taken, the excessive  
440 black body radiation coming from the furnace needs to be filtered, otherwise  
441 the image is oversaturated and presents no contrast. This is frequently achieved  
442 by using blue band pass filters, and sometimes neutral density filters depending  
443 on the exposure time of the pictures, that only allows that the blue part of the  
444 light spectrum arrives at the camera sensors. To increase the quality of the  
445 pictures, it is also common to enlighten the sample using a blue light source.

446 Figure 15 shows the experimental setup used to perform the Brazilian tests  
447 and to take the pictures at high temperatures. This setup is composed of the  
448 following parts:

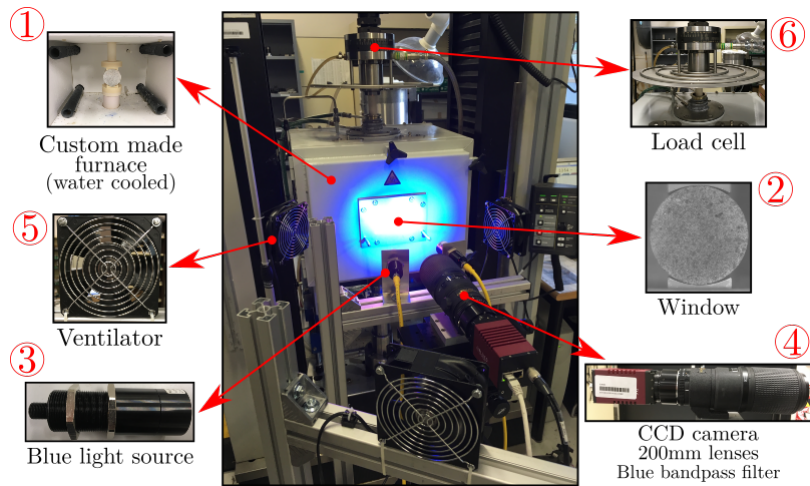


Figure 15: Experimental setup for the Brazilian tests at high temperature

- 449 1. A water cooled custom made furnace with the capacity to heat up to  
450 1300 °C.
- 451 2. The furnace's door is equipped with a window made of a vitro ceramic ma-  
452 terial, so that the sample can be photographed. This material was chosen  
453 because of its adequate resistance to temperatures up to 1300 °C, its low  
454 thermal expansion and its inexpensive price. The material is transparent  
455 enough to allow that satisfactory pictures are taken.
- 456 3. To increase the amount of blue light available when taking the pictures,  
457 two blue light sources are used to enlighten the sample. In combination  
458 with the blue filters, this increases significantly the contrast of the pictures,  
459 to a point where the DIC analysis becomes possible. These lights are  
460 mounted in a dedicated support that was designed to offers six degrees of  
461 freedom, so they can be easily positioned to avoid glare in the pictures.
- 462 4. A high resolution 12 bit CCD camera, AF Micro-Nikkor 200 mm lenses  
463 and a blue band pass filter, to decrease the amount of light being captured  
464 by the camera, since it blocks all parts of the optical spectrum that are  
465 not blue, avoiding the saturation of the sensor.
- 466 5. The camera and the lenses are cooled using two ventilators, since they  
467 stand close to the furnace and can overheat. A third ventilator is used to  
468 blow away the hot air between the window and the lenses, minimizing the  
469 generation of heat hazes.
- 470 6. A load cell with maximum capacity of 30 kN.

471 The samples used in the Brazilian tests were cut from parallel refractory  
472 bricks. The first step was to cut slices 40 mm thick, to guarantee the parallelism  
473 of the sample surface exposed to the camera. Second, 50 mm cylinders were  
474 drilled from these slices. This geometry was chosen to comply with a rule of  
475 thumb on the refractories field that requires the minimum dimension of the  
476 sample to be at least 10 times the size of the largest grain in the material, that,  
477 in the case of the alumina-spinel brick, is 3 mm.

478 To improve the contrast of the samples surfaces, a *SiC* powder speckle pat-

479 tern was used, with grain sizes varying from 50  $\mu\text{m}$  to 100  $\mu\text{m}$ . The surfaces of  
480 the sample were covered with a bonding agent, and the powder was deposited  
481 using a sieve, similar to what was done by Archer et al. (2020), what allowed a  
482 reasonable control over the particles dispersion. Using this method, the speckle  
483 does not remain strongly attached to the sample, and, even if it does not detach  
484 under simple gravitational action, direct contact with it should be avoided. Be-  
485 fore the test, the sample was let at rest for 12 hours, in order to dry the excess  
486 of the bonding agent. Figure 17a shows an example of a sample coated with a  
487 speckle pattern, already positioned at the testing machine.

488 To guarantee the good quality of the pictures, a rigorous procedure was  
489 followed at each test. This procedure was composed of:

- 490 1. The sample and the jaws were positioned at the testing machine at room  
491 temperature, and an initial pre-load of approximately 50 N was applied.
- 492 2. The furnace was closed, and the heating of the sample started. Figure 16  
493 shows the heating curves used for the tests. Between room temperature  
494 and 600 °C, a heating rate of 10 °C/min was used. From 600 °C to 1300  
495 °C, this rate was reduced to 5 °C, to avoid thermal damage on the sample  
496 and on the equipment. Before the beginning of the test, the furnace was  
497 let in a dwell for 1 h, to stabilize the temperature of the testing setup.  
498 The blue curve on Figure 16, obtained from one of the tests made at 1300  
499 °C, shows that the displacement of the machine piston was constant before  
500 the end of the dwell, indicating that there was no extra thermal expansion  
501 of the equipment at the beginning of the test.
- 502 3. After the temperature homogenization time was passed, the camera lenses  
503 and the blue band pass filter were cleaned to remove any dust particles  
504 that could cause artifacts in the pictures and later mounted on the camera.  
505 To increase the images contrast, the blue lights were positioned to generate  
506 the maximum illumination of the sample as possible, avoiding glare, and  
507 the focus was manually adjusted in order to increase the sharpness. The  
508 exposure time was adjusted according to the lightning conditions to avoid

509 too bright or too dark images.  
 510 4. The sample was loaded at a rate of 0.5 mm/min until the creep load was  
 511 achieved, and the force was held constant until the end of the test.

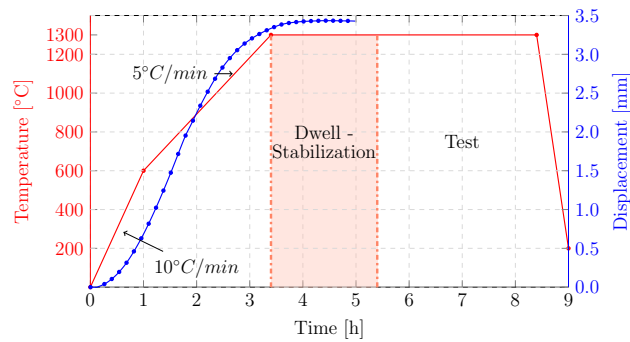


Figure 16: Heating curve and evolution of machine displacements prior to the test.

512 Figure 17 shows the effect of the lightning and of the blue band pass filter  
 513 in the quality of the images. At room temperature (Figure 17a), the histogram  
 514 of the image, shown in Figure 18, is approximately normally distributed around  
 515 gray values from 75 to 200, and the image presents a high contrast. At 1200 °C,  
 516 without the use of the blue lights and of the blue band pass filter (Figure 17b),  
 517 the distribution of gray levels is restricted to the range between 105 and 115,  
 518 and the images loses most of its contrast. The use only of the blue band pass  
 519 filter, without the blue lights (Figure 17c), slightly decreases the sharpness of  
 520 the histogram, but not enough to guarantee enough contrast. Finally, using the  
 521 blue lights and filter (Figure 17d), the gray level distribution becomes closer to  
 522 that of the image at room temperature, and most of the contrast is recovered.

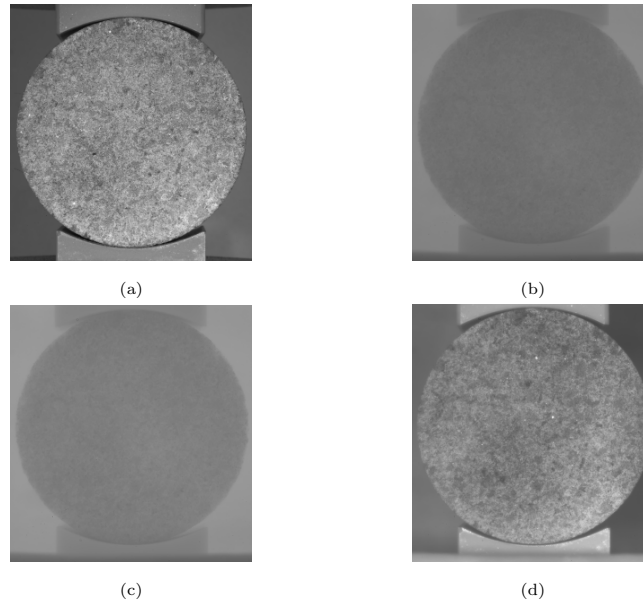


Figure 17: Influence of the blue light and the blue band pass filter in the quality of the image. (a) Image at room temperature. (b) No blue light and no filter. (c) No filter. (d) Use of blue light and blue band pass filter.

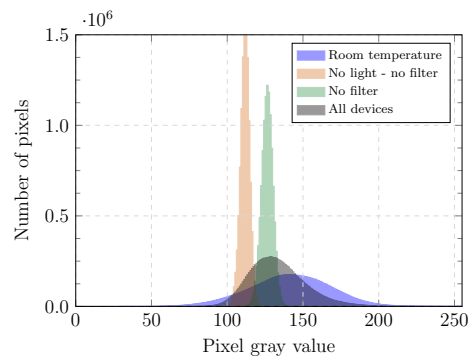


Figure 18: Histograms of the images at room and high temperature.

523 The open-source DIC software Ncorr (Blaber et al., 2015) was used to calcu-

524 late the full field displacements of the samples. Ncorr uses the local subset-based  
 525 reliability-guided DIC method according to Pan (2009).

526 **6. Identification of the asymmetric creep properties for the alumina-**  
 527 **spinel material at 1300 °C**

528 Figure 19 shows the relative vertical displacement of the upper point of the  
 529 Brazilian test samples at 1300 °C, calculated using DIC, that corresponds to  
 530 the difference between the vertical displacements at the upper part and the  
 531 vertical displacements at the lower part, to account for rigid body movements  
 532 of the experimental setup. It is possible to observe that samples 1, 3, 5 and  
 533 6 are in good agreement, while samples 2 and 4 are lower and upper outliers,  
 534 respectively.

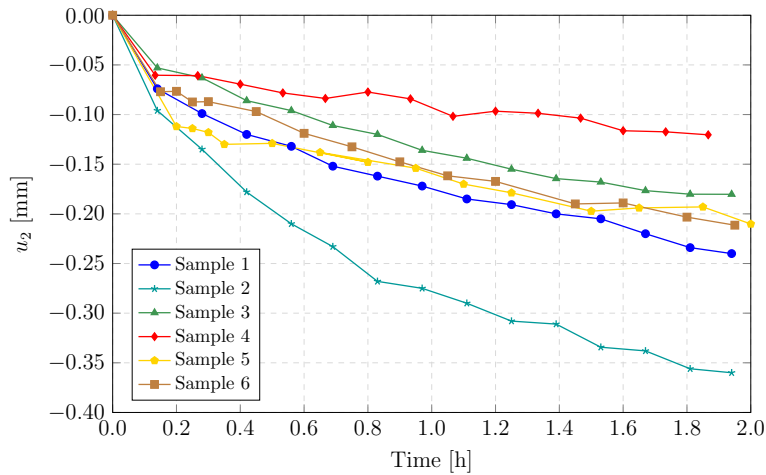


Figure 19: Brazilian tests time vs displacement curves obtained by DIC.

535 Figure 20 shows an example of envelope for the material parameters at  
 536 1300 °C, obtained through a series of numerical simulations using the asym-  
 537 metric creep model presented in Section 3. It can be expected that the material  
 538 parameters will not highly deviate from the ones presented in the figure, even



539 if this analysis only considers a single displacement value, and not the full field.

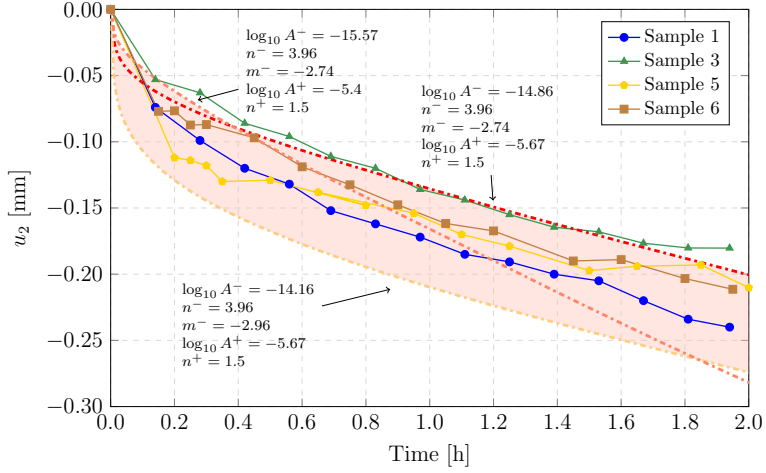


Figure 20: Brazilian tests time vs displacement curves and parameters envelope.

540 Finally, taking into account the influence of the material parameters in each  
 541 portion of the time vs displacement curve for Brazilian tests presented in Sec-  
 542 tion 4.2.1, the parameters for the alumina-spinel material were identified in  
 543 order to better approximate the values of the DIC calculations, and the result-  
 544 ing curve is presented in Figure 21. The identified parameters are shown in  
 545 Table 3.

Table 3: Identified material parameters

Parameter	Compression	Tension
$\log_{10} A [\text{MPa}^{-n} \text{s}^{-1}]$	-14.86	-5.55
$n [-]$	3.96	1.5
$m [-]$	-2.74	-

546 From Figure 21 it is possible to observe that the identified curve fits the

547 experimental values with good accuracy. The full DIC displacement field of  
 548 sample 6 was compared with the results of numerical simulations performed  
 549 using the identified material parameters, to verify the robustness of the identi-  
 550 fication.

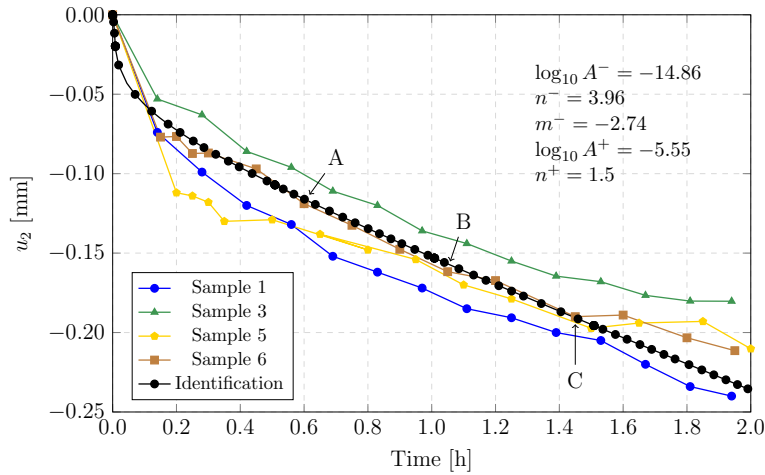


Figure 21: Brazilian tests time vs displacement curves and inverse identification.

551 The vertical displacements fields of Points A, B and C represented in Fig-  
 552 ure 21, corresponding to  $t = 0.6$  h,  $t = 1.05$  h and  $t = 1.45$  h, respectively, are  
 553 shown in Figure 22. It is possible to see that there is a rigid body rotation of  
 554 the sample, since the displacements map does not correspond to the traditional  
 555 displacements field of Brazilian tests. To consider this effect, an extra identifica-  
 556 tion calculation was made to determine what is the magnitude of the load that  
 557 caused this deviation. An horizontal load of  $-7$  N was identified and applied  
 558 on the upper jaws in the simulation model. This corresponds to an error of  $0.5^\circ$   
 559 in the application of the load, which shows that the experimental procedure is  
 560 sensitive to small deviations from the ideal boundary conditions.

561 Figure 23 shows the results of the numerical simulations using the previ-  
 562 ously identified material parameters and the horizontal load. It is possible to  
 563 observe that the displacement maps of Figures 22 and 23 have a good equiv-

564 alence, despite the experimental errors and the simplicity of the identification  
 565 procedure.

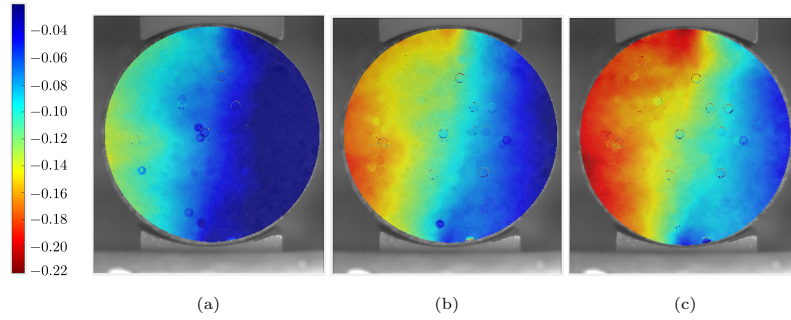


Figure 22: Brazilian tests: Vertical displacement in mm at 1300 °C – DIC sample 6. (a) Point A. (b) Point B. (c) Point C.

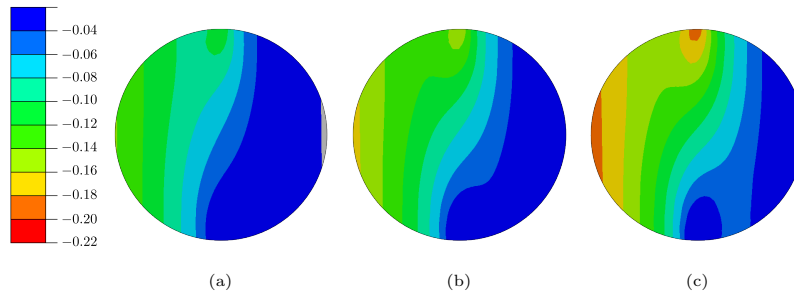


Figure 23: Brazilian tests: Vertical displacement in mm at 1300 °C – Simulation. (a) Point A. (b) Point B. (c) Point C.

566 It is interesting to observe how the vertical displacement of the central line  
 567 of the sample changes when the rigid body motions are included in the simulation,  
 568 as shown in Figure 24. When the boundary conditions are symmetric, the  
 569 displacement increases monotonically and equally in both sides of the sample,  
 570 as expected. Nevertheless, a horizontal force in the negative  $x$  direction causes  
 571 an increase in the magnitude of the displacements at the right side of the sam-  
 572 ple (point A in Figure 24), while the left side presents a positive displacement  
 573 during loading (point B in Figure 24). After approximately 1 h of creep defor-

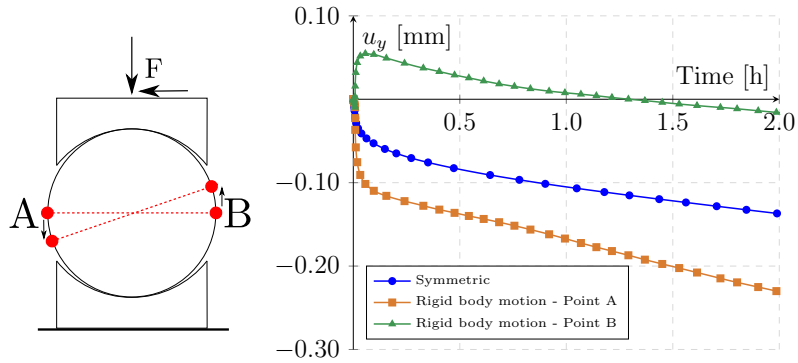


Figure 24: Brazilian tests: Vertical displacement of points A and B.

574 mations, the displacement of the right side becomes negative again, but always  
 575 smaller than at the left. This non-symmetric behavior, [caused by imperfections](#)  
 576 [in the boundary and loading conditions](#), is frequently observed in mechanical  
 577 experiments (de Melo et al., 2020) and has the potential to negatively influence  
 578 the DIC identifications if not properly considered.

## 579 7. Conclusions

580 From previous publications available in the literature, it is clear that refrac-  
 581 tory materials present a different creep behavior under tension and compression.  
 582 Therefore, there is a need to develop a dedicated model, considering that this  
 583 feature is not currently available in the main commercial Finite Element Anal-  
 584 ysis software. In the present work, an asymmetric creep model was proposed,  
 585 that was especially designed to simulate refractory materials at high temper-  
 586 atures. In comparison to previously published works, the proposed model has  
 587 the advantage to be able to represent the primary and secondary creep behavior  
 588 of the material, while keeping the possibility to have independent tests for the  
 589 identification of tension and compression parameters.

590 The main strategy employed in the development of the model was the split  
 591 of the stress tensor into a positive and a negative part, similar to what have

592 been done by Blond et al. (2005), but averaging the contributions of each stress  
593 sign by the equivalent stresses. In this case, the model tends to its symmetric  
594 version when the same material properties are used for both signs.

595 To identify the material parameters of an alumina-spinel material at 1300 °C,  
596 an experimental procedure composed of a Brazilian test in combination with a  
597 subset-based DIC technique was developed, that avoids the problems related  
598 to contact instrumentation at high temperatures. This technique showed to be  
599 successful for the determination of the model parameters.

## 600 Acknowledgments

601 This work was supported by the funding scheme of the European Com-  
602 mission, Marie Skłodowska-Curie Actions Innovative Training Networks in the  
603 frame of the project ATHOR - Advanced THERmomechanical multiscale mOD-  
604 elling of Refractory linings 764987 Grant. The authors acknowledge the com-  
605 pany RHI Magnesita for providing the alumina-spinel material.

## 606 References

- 607 Altenbach, H. (2001). Consideration of Stress State Influences in the Material  
608 Modelling of Creep and Damage. In S. Murakami & N. Ohno (Eds.),  
609 *IUTAM Symposium on Creep in Structures* (pp. 141–150). Springer  
610 Netherlands. [https://doi.org/10.1007/978-94-015-9628-2\\_15](https://doi.org/10.1007/978-94-015-9628-2_15)
- 611 Archer, T., Beauchêne, P., Huchette, C., & Hild, F. (2020). Global digital image  
612 correlation up to very high temperatures with grey level corrections.  
613 *Measurement Science and Technology*, *31*(2), 024003. [https://doi.org/](https://doi.org/10.1088/1361-6501/ab461e)  
614 [10.1088/1361-6501/ab461e](https://doi.org/10.1088/1361-6501/ab461e)
- 615 Banerjee, S. (2004). Properties of Refractories. *Refractories Handbook* (First,  
616 pp. 1–10). Marcel Dekker, Inc.

- 617 Belrhiti, Y., Dupre, J., Pop, O., Germaneau, A., Doumalin, P., Huger, M., &  
618 Chotard, T. (2017). Combination of Brazilian test and digital image cor-  
619 relation for mechanical characterization of refractory materials. *Journal*  
620 *of the European Ceramic Society*, 37(5), 2285–2293. [https://doi.org/](https://doi.org/10.1016/j.jeurceramsoc.2016.12.032)  
621 10.1016/j.jeurceramsoc.2016.12.032
- 622 Benallal, A., Billardon, R., & Doghri, I. (1988). An integration algorithm and the  
623 corresponding consistent tangent operator for fully coupled elastoplastic  
624 and damage equations. *Communications in Applied Numerical Methods*,  
625 4(6), 731–740. <https://doi.org/10.1002/cnm.1630040606>
- 626 Blaber, J., Adair, B., & Antoniou, A. (2015). Ncorr: Open-Source 2D Digital  
627 Image Correlation Matlab Software. *Experimental Mechanics*, 55(6),  
628 1105–1122. <https://doi.org/10.1007/s11340-015-0009-1>
- 629 Blond, E., Schmitt, N., Hild, F., Blumenfeld, P., & Poirier, J. (2005). Modelling  
630 of high temperature asymmetric creep behavior of ceramics. *Journal of*  
631 *the European Ceramic Society*, 25(11), 1819–1827. [https://doi.org/10.](https://doi.org/10.1016/j.jeurceramsoc.2004.06.004)  
632 1016/j.jeurceramsoc.2004.06.004
- 633 Darvell, B. W. (1990). Uniaxial compression tests and the validity of indirect  
634 tensile strength. *Journal of Materials Science*, 25(2), 757–780. [https:](https://doi.org/10.1007/BF03372161)  
635 [//doi.org/10.1007/BF03372161](https://doi.org/10.1007/BF03372161)
- 636 de Melo, C. C., Furlan, M., Hild, F., Schmitt, N., & Canto, R. B. (2020). Uniaxial  
637 compression test on ceramic green compact with bending consideration  
638 using digital image correlation. *Powder Technology*, 376, 136–148. [https:](https://doi.org/10.1016/j.powtec.2020.08.002)  
639 [//doi.org/10.1016/j.powtec.2020.08.002](https://doi.org/10.1016/j.powtec.2020.08.002)
- 640 Dutta, S. K., & Chokshi, Y. B. (2020). *Basic Concepts of Iron and Steel Making*.  
641 Springer Singapore. <https://doi.org/10.1007/978-981-15-2437-0>
- 642 Esposito, L., & Bonora, N. (2011). A primary creep model for Class M materials.  
643 *Materials Science and Engineering: A*, 528(16-17), 5496–5501. [https:](https://doi.org/10.1016/j.msea.2011.03.069)  
644 [//doi.org/10.1016/j.msea.2011.03.069](https://doi.org/10.1016/j.msea.2011.03.069)
- 645 Fahad, M. K. (1996). Stresses and failure in the diametral compression test.  
646 *Journal of Materials Science*, 31(14), 3723–3729. [https://doi.org/10.](https://doi.org/10.1007/BF00352786)  
647 1007/BF00352786

- 648 Fairhurst, C. (1964). On the validity of the ‘Brazilian’ test for brittle materials.  
649 *International Journal of Rock Mechanics and Mining Sciences & Ge-*  
650 *omechanics Abstracts*, 1(4), 535–546. [https://doi.org/10.1016/0148-](https://doi.org/10.1016/0148-9062(64)90060-9)  
651 [9062\(64\)90060-9](https://doi.org/10.1016/0148-9062(64)90060-9)
- 652 García, V. J., Márquez, C. O., Zúñiga-Suárez, A. R., Zuñiga-Torres, B. C.,  
653 & Villalta-Granda, L. J. (2017). Brazilian Test of Concrete Specimens  
654 Subjected to Different Loading Geometries: Review and New Insights.  
655 *International Journal of Concrete Structures and Materials*, 11(2), 343–  
656 363. <https://doi.org/10.1007/s40069-017-0194-7>
- 657 Gazeau, C., Gillibert, J., Blond, E., Geffroy, P.-M., & Richet, N. (2015). Exper-  
658 imental set up for the mechanical characterization of plane ITM mem-  
659 brane at high temperature. *Journal of the European Ceramic Society*,  
660 35(14), 3853–3861. <https://doi.org/10.1016/j.jeurceramsoc.2015.06.026>
- 661 Jin, S., Harmuth, H., & Gruber, D. (2014). Compressive creep testing of re-  
662 fractories at elevated loads - Device, material law and evaluation tech-  
663 niques. *Journal of the European Ceramic Society*, 34(15), 4037–4042.  
664 <https://doi.org/10.1016/j.jeurceramsoc.2014.05.034>
- 665 Jin, S., Harmuth, H., Gruber, D., & Rössler, R. (2015). Influence Of Creep  
666 On The Thermomechanical Behavior Of a RH-Snorkel. *Unified Inter-*  
667 *national Technical Conference on Refractories*, 4.
- 668 Jin, S., Harmuth, H., Gruber, D., Buhr, A., Sinnema, S., & Rebouillat, L. (2020).  
669 Thermomechanical modelling of a torpedo car by considering working  
670 lining spalling. *Ironmaking & Steelmaking*, 47(2), 145–149. [https://doi.](https://doi.org/10.1080/03019233.2018.1495797)  
671 [org/10.1080/03019233.2018.1495797](https://doi.org/10.1080/03019233.2018.1495797)
- 672 Jin, S., Harmuth, H., Gruber, D., & Li, Y. (2011). Classification of Thermome-  
673 chanical Impact Factors and Prediction Model for Ladle Preheating. *J*  
674 *Wuhan Univ Sci Technol*, 34, 8.
- 675 Lemaître, J., & Chaboche, J. (1990). *Mechanics of solid materials*. Cambridge  
676 University Press.
- 677 Leplay, P., Lafforgue, O., & Hild, F. (2015). Analysis of Asymmetrical Creep  
678 of a Ceramic at 1350°C by Digital Image Correlation. *Journal of the*

- 679 *American Ceramic Society*, 98(7), 2240–2247. <https://doi.org/10.1111/jace.13601>
- 680
- 681 Leplay, P., Réthoré, J., Meille, S., & Baietto, M.-C. (2010). Damage law identification of a quasi brittle ceramic from a bending test using Digital
- 682 Image Correlation. *Journal of the European Ceramic Society*, 30(13),
- 683 2715–2725. <https://doi.org/10.1016/j.jeurceramsoc.2010.05.021>
- 684
- 685 Leplay, P., Réthoré, J., Meille, S., & Baietto, M.-C. (2012). Identification of
- 686 asymmetric constitutive laws at high temperature based on Digital
- 687 Image Correlation. *Journal of the European Ceramic Society*, 32(15),
- 688 3949–3958. <https://doi.org/10.1016/j.jeurceramsoc.2012.03.024>
- 689 Mahnken, R. (2003). Creep simulation of asymmetric effects by use of stress
- 690 mode dependent weighting functions. *International Journal of Solids*
- 691 *and Structures*, 40(22), 6189–6209. [https://doi.org/10.1016/S0020-](https://doi.org/10.1016/S0020-7683(03)00388-3)
- 692 [7683\(03\)00388-3](https://doi.org/10.1016/S0020-7683(03)00388-3)
- 693 Naumenko, K., & Altenbach, H. (2007). *Modeling of Creep for Structural Analysis* (V. I. Babitsky & J. Wittenburg, Eds.). Springer Berlin Heidelberg.
- 694 <https://doi.org/10.1007/978-3-540-70839-1>
- 695
- 696 Novak, M. D., & Zok, F. W. (2011). High-temperature materials testing with
- 697 full-field strain measurement: Experimental design and practice. *Review*
- 698 *of Scientific Instruments*, 82(11), 115101. [https://doi.org/10.1063/1.](https://doi.org/10.1063/1.3657835)
- 699 [3657835](https://doi.org/10.1063/1.3657835)
- 700 Pan, B. (2009). Reliability-guided digital image correlation for image deformation
- 701 measurement. *Applied Optics*, 48(8), 1535. [https://doi.org/10.](https://doi.org/10.1364/AO.48.001535)
- 702 [1364/AO.48.001535](https://doi.org/10.1364/AO.48.001535)
- 703 Samadi, S., Jin, S., Gruber, D., Harmuth, H., & Schachner, S. (2020). Statistical
- 704 study of compressive creep parameters of an alumina spinel refractory.
- 705 *Ceramics International*, 46(10, Part A), 14662–14668. [https://doi.org/](https://doi.org/10.1016/j.ceramint.2020.02.267)
- 706 [10.1016/j.ceramint.2020.02.267](https://doi.org/10.1016/j.ceramint.2020.02.267)
- 707 Samadi, S., Jin, S., & Harmuth, H. (2021). Combined damaged elasticity and
- 708 creep modeling of ceramics with wedge splitting tests. *Ceramics Inter-*



709           *national*, 47(18), 25846–25853. [https://doi.org/10.1016/j.ceramint.](https://doi.org/10.1016/j.ceramint.2021.05.315)  
710           2021.05.315

711 Schachner, S., Jin, S., Gruber, D., & Harmuth, H. (2019). Three stage creep  
712           behavior of MgO containing ordinary refractories in tension and com-  
713           pression. *Ceramics International*, 45(7), 9483–9490. [https://doi.org/](https://doi.org/10.1016/j.ceramint.2018.09.124)  
714           10.1016/j.ceramint.2018.09.124

715 Schacht, C. A. (2004). Thermomechanical Considerations for Refractory Lin-  
716           ings. *Refractories Handbook* (First, pp. 369–394). Marcel Dekker, Inc.

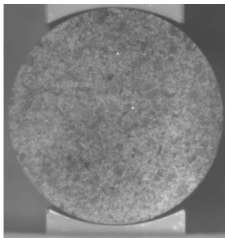
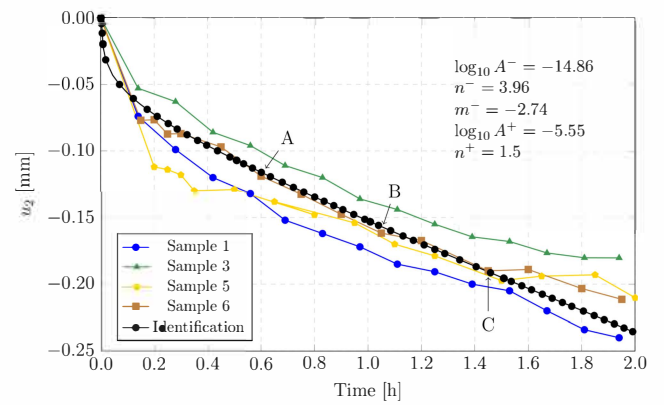
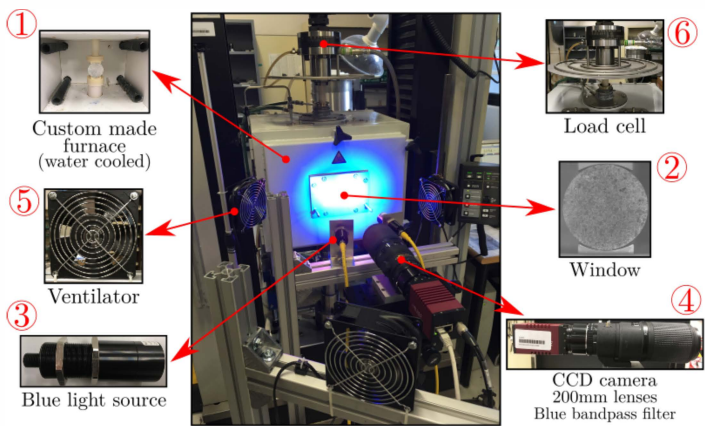
717 Sidi Mammar, A., Gruber, D., Harmuth, H., & Jin, S. (2016). Tensile creep  
718           measurements of ordinary ceramic refractories at service related loads  
719           including setup, creep law, testing and evaluation procedures. *Ceramics*  
720           *International*, 42(6), 6791–6799. [https://doi.org/10.1016/j.ceramint.](https://doi.org/10.1016/j.ceramint.2016.01.056)  
721           2016.01.056

722 Teixeira, L., Samadi, S., Gillibert, J., Jin, S., Sayet, T., Gruber, D., & Blond,  
723           E. (2020). Experimental Investigation of the Tension and Compression  
724           Creep Behavior of Alumina-Spinel Refractories at High Temperatures.  
725           *Ceramics*, 3(3), 372–383. <https://doi.org/10.3390/ceramics3030033>

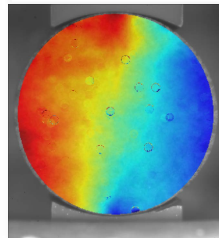
726 Volkova, O., & Janke, D. (2005). Influence of the Lining on the Thermal Be-  
727           haviour of a Teeming Ladle. *steel research international*, 76(4), 313–  
728           319. <https://doi.org/10.1002/srin.200506014>  
729           \_eprint: <https://onlinelibrary.wiley.com/doi/pdf/10.1002/srin.200506014>

## Highlights

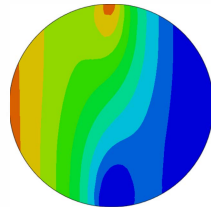
- A creep model is proposed to represent the asymmetric behavior of refractories.
- The influences of each stress sign are weighted using a split of the stress tensor.
- The model can represent primary and secondary creep strain rates.
- A Brazilian test and a DIC analysis are used in the mechanical characterization.
- A refractory used in steel production is characterized using the proposed method.



Speckle pattern  
at 1300 °C



Digital Image Correlation  
analysis



Numerical Simulation

### Conclusion:

In this work, a new creep model to simulate refractory materials was proposed, that can represent the material's asymmetric behavior, i.e., different properties under tension and compression. The model parameter can be fully identified using a Brazilian test in combination with a Digital Image Correlation technique. An experimental setup to acquire high quality images at high temperatures is also proposed.

**Lucas Teixeira:** Conceptualization, Methodology, Software, Validation, Writing - Original Draft **Jean Gillibert:** Resources, Supervision. **Thomas Sayet:** Resources, Supervision, Writing - Review & Editing . **Eric Blond:** Resources, Supervision, Writing - Review & Editing.

**Declaration of interests**

The authors declare that they have no known competing financial interests or personal relationships that could have appeared to influence the work reported in this paper.

The authors declare the following financial interests/personal relationships which may be considered as potential competing interests:

Lucas Breder Teixeira reports financial support was provided by EU Framework Programme for Research and Innovation Marie Skłodowska-Curie Actions.